Attenuation estimation from DAS VSP data of CaMI Field Research Station

Yichuan Wang and Don C. Lawton

ABSTRACT

For seismic monitoring injected CO_2 during geologic CO_2 sequestration, it is useful to measure seismic attenuation. Seismic attenuation directly connects to different petrophysical parameters of reservoir rock or CO_2 capture and storage site. We have used an approach for measuring attenuation by iteratively identifying a sparse set of the strongest reflections in the seismic trace and stacking their waveforms. This method is straightforward and requires no sophisticated inverse algorithm. It is data-driven and shows a trade-off between resolution and estimation accuracy. This method is applied to the DAS VSP dataset from the CaMI Field Research Station (FRS) in Newell County, Alberta. High-quality attenuation-quantity cross-sections are obtained. Strong attenuation within the CO_2 injection zone around the CO_2 injection well is observed, which is interpreted as being related to the injected CO_2 at the FRS.

INTRODUCTION

Seismic attenuation causes wave-amplitude decay during seismic wave propagation. The overall effect is the amplitude of high-frequency component attenuates more rapidly than that of the low-frequency component. This leads to the loss of signal resolution and brings difficulties in geologic mapping and interpretation. However, we can also measure and make use of the attenuation for different geophysical purposes. Compared with velocity or density, attenuation is often more sensitive to changes in clay content, gas or water saturation, permeability, pore fluid, and microfracturing. After attenuation measurement, seismic inverse Q filtering can be performed for the compensation of resolution loss and improve seismic interpretation.

Attenuation was estimated from different kinds of data such as vertical seismic profile (VSP) (Tonn, 1991), crosswell (Neep et al., 1996), sonic log (Sun et al., 2000) or the drift between check-shot and sonic trave time (Carter et al., 2020). The task of estimating attenuation attributes by using distributed acoustic sensing (DAS) VSP records for monitoring injected CO_2 is considered in this report. There are many different methods for attenuation estimation in either time or frequency domain. The frequency-domain methods for attenuation estimation are general in exploration seismology due to their robustness and ease of use. Estimation of amplitude spectra is required for frequency-domain methods. In this report, attenuation is measured from the logarithmic spectral ratio of the time-frequency variant amplitude. We apply Wang and Morozov's (2020) approach to calculate such 2D spectrogram by iterative identification of locally strongest reflections and stacking their waveforms within different windows along a seismic trace (see the "Attenuation measurement from sparse strongest reflections" subsection).

The spectral ratio method is widely used in practice, but also susceptible to background random noise (Tonn, 1991) and thin layer (O'Doherty and Anstey, 1971). The thin-layer effect could introduce notches into amplitude spectra and make the spectral ratio

measurement to be bandwidth dependent and introduce bias into estimated results. Different techniques have been proposed to be combined with the spectral ratio method for reducing these effects, such as the time-frequency transforms (Reine et al., 2009) or layer stripping method (Behura and Tsvankin, 2009). Compared with these improvements, the approach in this report needs no hypothetical model and uses no sophisticated inverse algorithm, and consequently requires less subjective parameters. This data-driven approach also needs a certain length of data segment for analysis as there is a trade-off between resolution and accuracy (White, 1992; see the "Discussion" section).

In the "Method" section, we show our attenuation-estimation procedures based on the sparse strongest reflections (Wang and Morozov, 2020). Besides measuring the frequency-dependent part of attenuation that is typically characterized by the $1/Q$, we also measure the quantity γ for geometric attenuation (Morozov, 2008). In the "Application" section, we demonstrate how the attenuation measurements from our approach help to identify injected CO_2 at CaMI Field Research Station (FRS).

DAS VSP at CaMI FRS

The CaMI FRS is located in Newell County, Alberta, about 200 km southeast of Calgary. At the CaMI FRS, we focus on the development of subsurface and surface measurement, monitoring and verification technologies for the carbon capture and storage (CCS). There are one CO_2 injection well and two observation wells (OBS1 and OBS2, Figure 1) at the FRS. The DAS VSP in this report was acquired on March 1st, 2021. Figure 1 shows the shot locations of one walk-around and three walk-away lines of this survey. This report measures the attenuation for the walk-away line 15, which is with the direction of northwest to southeast.
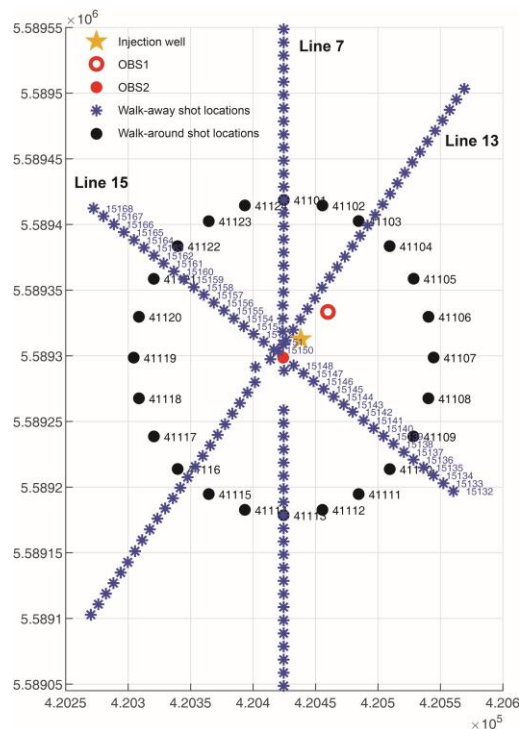

Figure 1. VSP layout map of Match 1st survey.

Different geophysical instruments are permanently installed at the FRS, such as DAS using straight and helical fibre optic cables with a continuous loop of about 5km in a horizontal trench and two observation wells (Lawton et al., 2019). Envirovibe was used as the source for the March 1st survey with two sweeps of 10 – 150 Hz over 16 s (0.25 s taper at the start and end) for each shot location. Figure 2 is an example of a raw DAS shot gather by summing the two sweeps. This report discusses the data portion from the down-loop and up-loop straight fiber of OBS2, indicated by the dashed lines in Figure 2.
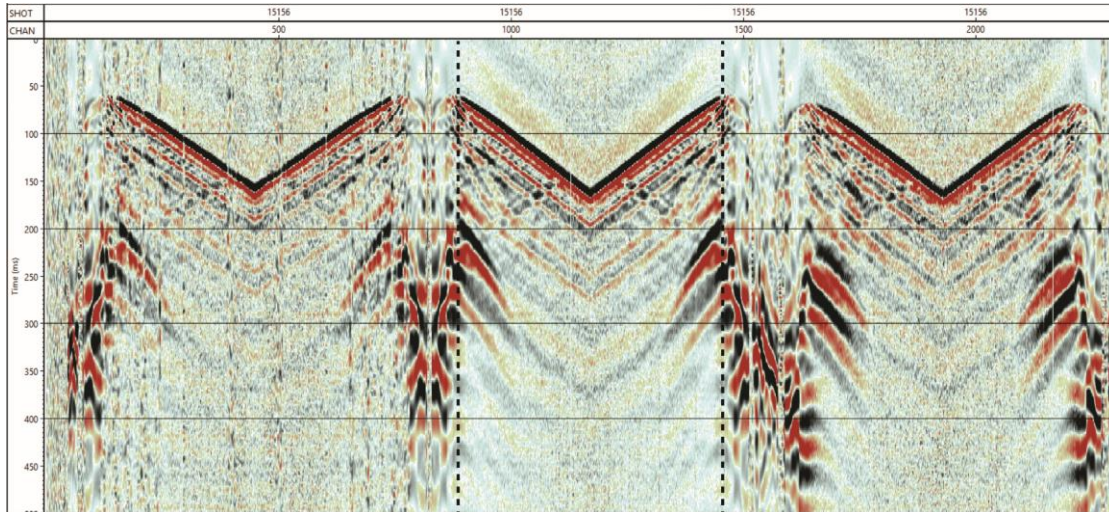

Figure 2. One DAS shot gather of March 1st survey.

Figure 3 shows the separation of upgoing (reflection) wavefield from the raw data of straight fiber of OBS2 by the median and FK filter. The Basal Belly River Sandstone Formation (BBRS) reflection of the injection zone of interest is indicated in Figure 3b. The BBRS at the FRS is a 7 m formation with a fine- to medium-grained sandstone. Its upper contact is at the depth of approximately 295 m.
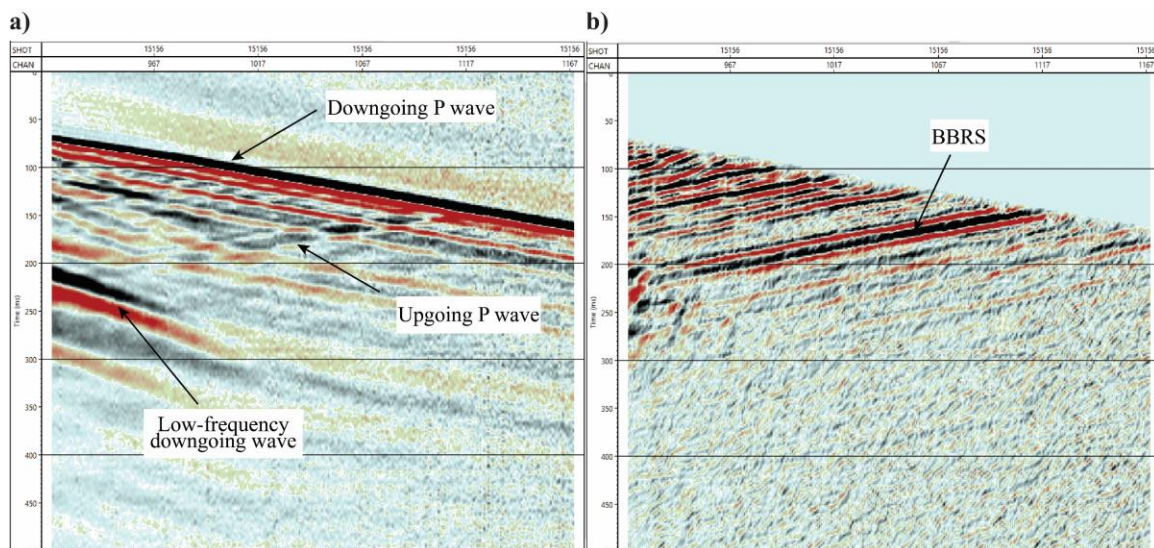

Figure 3. a) Raw DAS shot gather from the sum of data from down-loop and up-loop fiber in OBS2, and b) isolated P-wave upgoing waves.

METHOD

Seismic attenuation model

In the frequency domain, the non-stationary convolutional model for seismic reflection signal is given by

$$A(t,f) = A_0(t,f) F(t,f) G(t),\qquad(1)$$

where t is the time, f is the frequency, $A(t,f)$ is the time-frequency variant amplitude of the recorded signal, $A_0(t,f)$ is the $A(t,f)$ in the absence of attenuation and focusing/defocusing, $F(t,f)$ and $G(t)$ are the path effect (attenuation) on seismic amplitude.

For traveling waves whose amplitude exponentially decays with traveltime in relation 1, $F(t,f) = \exp\left[-\pi f \int_0^t d\tau / Q(\tau)\right]$ describes the frequency-dependent attenuation effect, and $G(t) = \exp\left[-\int_0^t \gamma(\tau) d\tau\right]$ corresponds to the geometric attenuation including small wavefront distortions and random scattering. The differential attenuation quantity γ is the natural counterpart of $1/Q$ and they should be measured simultaneously (Morozov, 2008). $A_0(t,f)$ in equation 1 is the product of source spectrum $S(f)$ and reflectivity time-frequency response $R(t,f)$:

$$A_0(t,f) = S(f) R(t,f).\qquad(2)$$

The effects of $S(f)$ and $R(t,f)$ are removed during the derivative of the logarithm of the spectral ratio for $A(t,f)$ and $A_0(t,f)$ from equation 1:

$$\frac{\partial\{\ln[A(t,f)/A_0(t,f)]\}}{\partial\tau} = -\gamma - \frac{\pi}{Q} f,\qquad(3)$$

by which a linear regression with frequency f is used to obtain the attenuation coefficient $1/Q$ and γ at time t.

Attenuation measurement from sparse strongest reflections

We follow Wang and Morozov's (2020) approach to obtain the $A(t,f)/A_0(t,f)$ in equation 3 for attenuation measurement by iteratively identifying a sparse set of the strongest reflections in the seismic trace and stacking their waveforms (Figure 4). The underlying physical hypothesis of this procedure focuses on the statistical properties of the seismograms recorded adjacent to locally strongest reflections rather than the statistical properties of the whole seismograms. For the measurement, a group of overlapping windows of length T_w centered at times t_i are extracted along a seismic trace (Figure 4a). Within each window number i, locally strongest reflection waveforms of length T_1 not closer than a length T are identified, normalized, and stacked to reduce the tunning effect (Figure 4b and 4c). Fourier amplitude spectra $A_i(t_i,f)$ is then obtained from the stacked waveform within each window. The spectra of stacked reflectivity (unknown) from this procedure within each window number i is donated as $R_i(t_i,f)$. By considering the $R_i(t_i,f)$

is stationary for a certain frequency range, the $A_{0i}(t_i, f) = R_i(t_i, f) S(f)$ from relation 2 would also be stationary and approximately estimated as the average of $A_i(t_i, f)$ at different times. The spectral ratio in equation 3 for the attenuation measurement would then be

$$\left. \frac{A(t, f)}{A_0(t, f)} \right|_{t=t_i} = \frac{A_i(t_i, f)}{A_{0i}(t_i, f)} \approx \frac{A_i(t_i, f)}{\overline{A}_i(t_i, f)}, \tag{4}$$

where $\overline{A}_i(t_i, f)$ denotes the mean value of $A_i(t_i, f)$ over all times t_i.
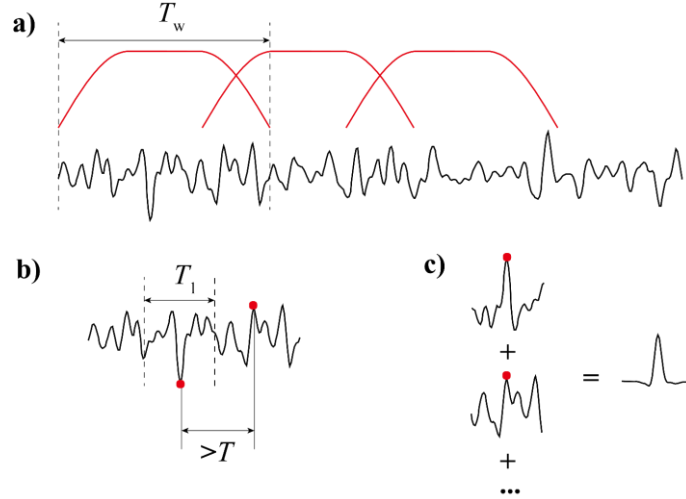

Figure 4. Sparse strongest reflections identification procedure: a) overlapping time windows (red curves) and seismic trace (black curve); b) selected strongest reflection waveforms (red dots); and c) normalization and stacking of the selected reflection waveforms.

During the practical measurement, the spectra $A_i(t_i, f)$ could be calculated for any trace at spatial position (x, y) within a seismic dataset, denoted as $A_i(t_i, f \mid x, y)$. We perform the locally weighted scatterplot smoothing (LOWESS) for the $A_i(t_i, f \mid x, y)$ values along time t_i and frequency f respectively to get a smooth spectrogram $\tilde{A}_i(t_i, f \mid x, y)$. By equation 4, the spectral ratio in equation 3 is approximated as $\tilde{A}_i(t_i, f \mid x, y) / \overline{\tilde{A}}_i(t_i, f \mid x, y)$. The $1/Q$ and γ values can then be estimated from the linear regression of $\partial \left\{ \ln \left[\tilde{A}_i(t_i, f \mid x, y) / \overline{\tilde{A}}_i(t_i, f \mid x, y) \right] \right\} / \partial \tau$ and frequency f as equation 3 with a selected frequency band of $[f_1, f_2]$. To further reduce the instability or errors of attenuation estimation, we perform another LOWESS along different traces (x, y) for the $1/Q$ or γ values. The $1/Q$ or γ cross-section or volume is then obtained by using a continuous curvature gridding with adjustable tension for the set of discrete values, by which $1/Q$ or γ values at the arbitrary times t_i and positions (x, y) are gridded with a surface having continuous second derivatives and curvature.

APPLICATION

We first apply the proposed attenuation-estimation method to synthetic seismograms built from sparse pulses. The synthetic attenuated seismogram is simulated from input reflectivity through seismic convolutional model with input wavelet and computing attenuation effects plus additive noise. Figure 5 shows the Ricker wavelet with the peak frequency of 40 Hz, and synthetic attenuated seismograms built from sparse pulses (spike reflectivity) by using this wavelet. In Figure 5b, the attenuated seismogram in the first left panel is noise free and the second to the fourth are with white Gaussian noise of signal-to-noise ratios (S/Ns) of 20, 10 and 5 dB, respectively. We separate the seismograms into two layers from 300 ms and apply no attenuation for the upper layer and constant $1/Q = 0.02$ and $\gamma = -2$ s^{-1} for the deeper layer. The resulting estimated attenuation coefficient can be directly compared with the input one, which allows evaluating the performance of the method. Figure 5c shows the amplitude spectra of synthetic seismograms without noise and of S/N = 5. The spectra are scaled to equal peak amplitude for the convenience of their comparison. The gray dashed lines in Figure 5c indicate the estimated top frequencies ($\sim$85 Hz) below which the synthetic seismograms without noise (red lines in Figure 5b) from Ricker can be considered dominant. Above these frequencies, the added white Gaussian noise dominates the synthetic seismograms of S/N = 5. We obtain the amplitude spectra from the two layers of Figure 5b separately. Without the performance of LOWESS for this case, the spectra of the first and second layers correspond to $A_0(t, f)$ and $A(t, f)$ in equation 3, respectively. $1/Q$ and γ are estimated from their spectral ratio.
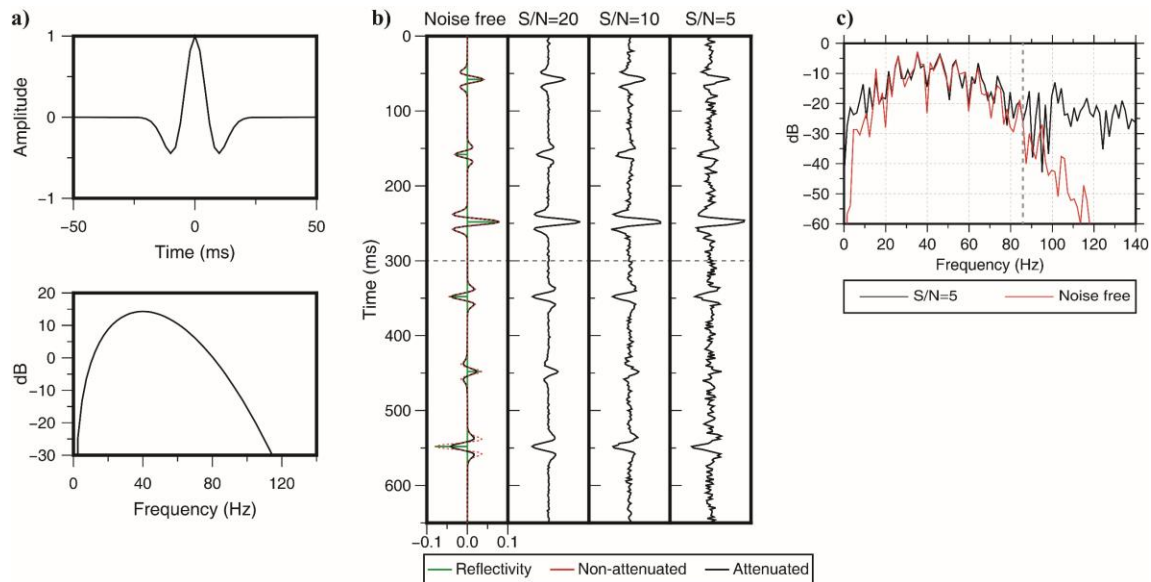

Figure 5. Synthetic model with constant $1/Q$ and γ. a) waveforms and amplitude spectra for Ricker; b) synthetic seismograms without and with different levels of white Gaussian noise (labeled at the top); c) amplitude spectra for synthetic seismograms. The spike reflectivity, non-attenuated and attenuated synthetic in the far-left panel of b) are indicated in the legend below.

We test the robustness of this attenuation estimation for noise with respect to the frequency bandwidth [f_1, f_2] used in the linear regression. In this test, the attenuation estimation is repeated for different bandwidths with the lower frequency ranging from 0 to 50 Hz and the upper frequency ranging from 70 to 130 Hz. For each bandwidth, we conduct

1000 independent realizations with added Gaussian random noise and use the mean value of the 1000 estimations as the estimated $1/Q$ and γ. The $1/Q$ and γ values for each bandwidth are plotted as Figure 6. In this figure, areas of $1/Q$ close to 0.02 or γ close to -2 s^{-1} indicate the stability of estimation for different frequency bandwidths.
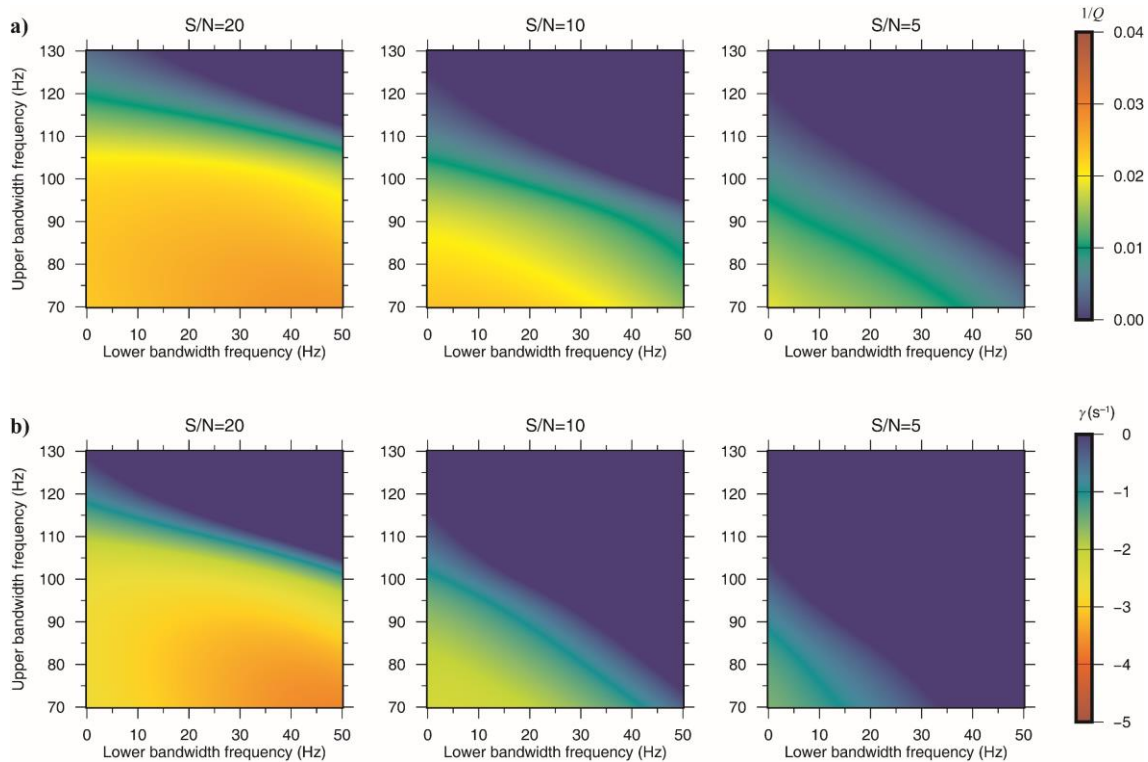

Figure 6. a) $1/Q$ values and b) γ values estimated from synthetic attenuated seismograms with different noise levels (labels) over a range of bandwidths.

With the result in Figure 6 and the amplitude spectra in Figure 5c, we can observe the stable areas of bandwidth selection for $1/Q$ estimation correlate with the dominant frequency band of synthetic seismogram. Although the stable areas decrease with the lowering of S/N in Figure 6a, the tests demonstrate the stability of our $1/Q$ estimation with frequency for linear regression within the entire dominant band of input wavelet (Figure 5a) or synthetic seismogram (Figure 5c). For γ estimation in Figure 6b, only the stable area of bandwidth selection of S/N = 5 for the case of Ricker is less than the dominant band of synthetic seismogram in Figure 5c. The comparison of Figure 6a with 6b shows there are fewer stable areas with the lowering of S/N for the γ estimation than the $1/Q$ estimation.

For an ideal situation, Figure 6 would show the same color for all the different bandwidths. However, spectral fluctuations caused by the added random noise lead the attenuation measurement from linear regression to be bandwidth-selection dependent. We therefore measure the $1/Q$ and γ with different bandwidths determined from Figure 6. For traces in Figure 5b built from Ricker wavelet with the S/N of 20, 10, and 5 dB, we measure the $1/Q$ with the bandwidths of 0–110 Hz, 0–100 Hz and 0–90 Hz and the γ with the bandwidths of 0–110 Hz, 0–90 Hz and 0–80 Hz. Figure 7 show the histograms of estimated $1/Q$ and γ with 1000 independent realizations at each S/N. The standard deviation (σ) is

much larger for the estimated γ in Figure 7b than the estimated $1/Q$ in Figure 7a and increases with the amount of noise for both. All the median values for estimated $1/Q$ in Figure 7 except the case of low S/N = 5 dB are larger than the input $1/Q$ of 0.02 by a lower order of magnitude, while the median values for estimated γ in Figure 7 is either smaller or larger than the input γ of -2 s^{-1} by much larger amounts. In summary, tests on synthetic seismograms show that 1) incoherent random noise makes the attenuation estimation bandwidth-dependent; 2) our attenuation-estimation method demonstrates its stability with different noise levels within the dominant frequency band; 3) the estimation of γ is more susceptible to noise than the estimation of $1/Q$.
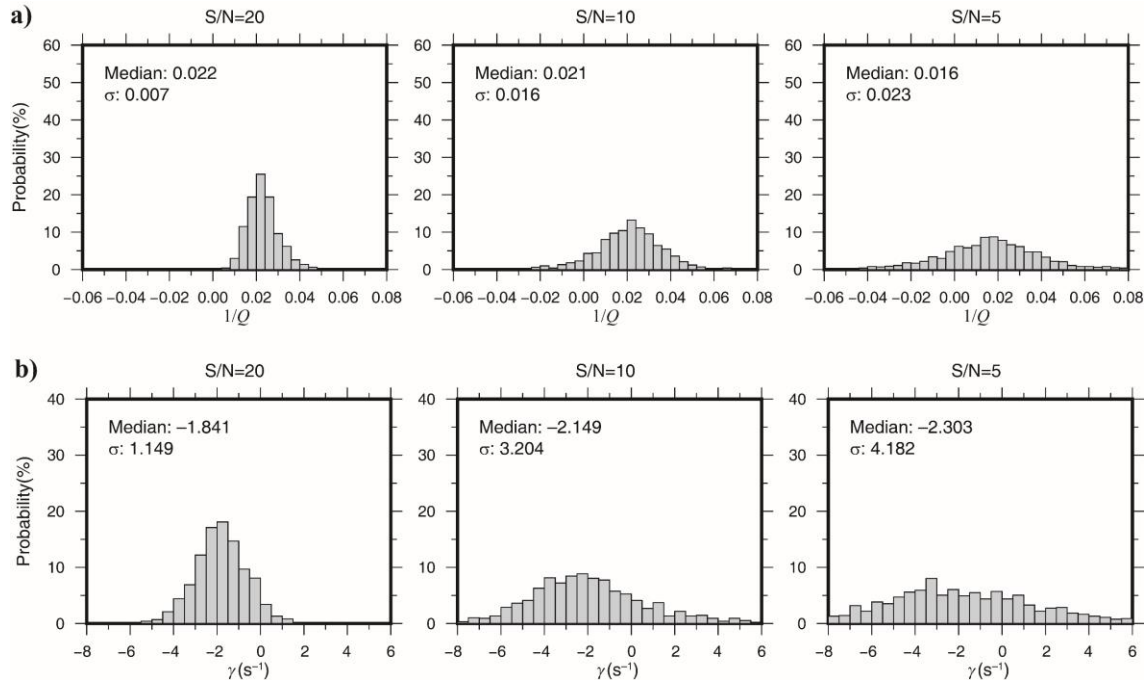

Figure 7. Histograms of the $1/Q$ and γ estimated from synthetic attenuated seismograms with different noise level (labels). The median values and standard deviations are labeled in each histogram.

Our seismic attenuation measurement is then applied to the VSP CDP stack of walkaway line 15 (Figure 1). The VSP CDP stack is obtained from the upgoing reflections of each shot gather as in Figure 3b. Figure 8 shows this VSP CDP stack of high quality with the BBRS reflection indicated, and the measured differential attenuation quantity $1/Q$ and γ. There were around accumulative 34 tonnes of CO_2 injected into the BBRS at the CaMI FRS until this DAS VSP acquisition date of March 1st 2021. According to the measurements as in Figure 8, the injected CO_2 at the FRS causes a strong attenuation around the injection well at the BBRS with the $1/Q$ values as high as about 0.12. This result shows that our approach can obtain stable attenuation measurement from field data such as DAS VSP, and the measurement from this approach is an advantageous indicator for the CCS monitoring.
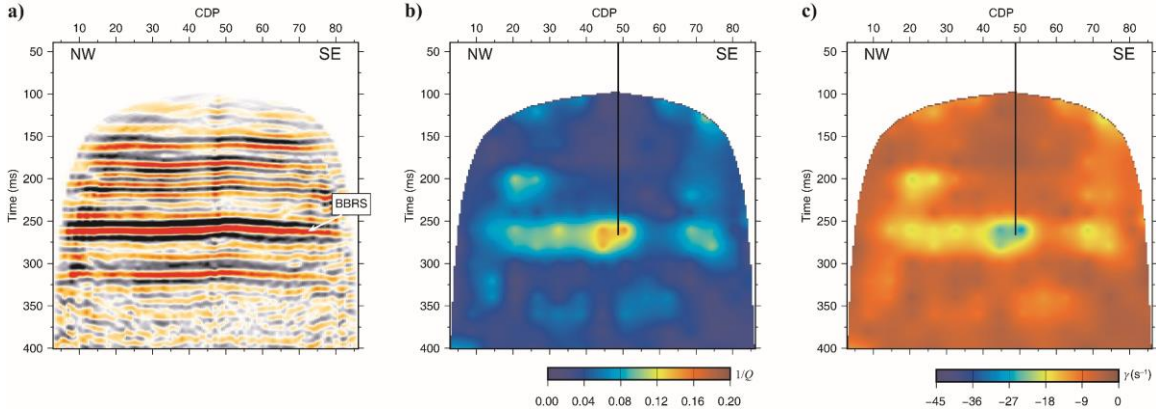
Figure 8. a) VSP CDP stack, b) estimated $1/Q$ values and c) estimated γ values. Black line in b) or c) indicates the location and depth of the CO_2 injection well at FRS.

DISCUSSION

We evaluate the accuracy of estimated $1/Q$ and γ by considering the temporal resolution. By sampling the amplitude spectra at M equidistant frequency width b within the bandwidth of $B = Mb = |f_1 - f_2|$, the attenuation coefficients derived by fitting the regression of spectral ratio and frequency in equation 3 are random values reliant on the spectral sampling and possess statistical bias. For recorded signal with a S/N that is much larger than one and measurements from independent time windows (Figure 4a), the relative variance of the spectral ratio is $\sigma^2 = 1/2bT_1N_1$ (White, 1992), where T_1 is the length of selected reflection waveforms (Figure 4b) and N_1 is the total number of amplitude peaks selected within each window. Considering this variance as constant over the measurement bandwidth and using the full frequency band ($B = Mb$), the relative standard error ($e = \sigma$) of Q and γ determined from equation 3 is (White, 1992)

$$e_Q = \sqrt{\frac{\mathrm{var}\{\hat{Q}\}}{Q^2}} \approx \frac{\sqrt{6}Q}{\pi T_{\mathrm{m}} B^{3/2} \left(T_1 N_1\right)^{1/2}} \text{ and } e_\gamma = \sqrt{\frac{\mathrm{var}\{\hat{\gamma}\}}{\gamma^2}} \approx \frac{1}{|\gamma| T_{\mathrm{m}} \left(2BT_1N_1\right)^{1/2}} . \quad (5)$$

where T_{m} is the time distance between the start positions of two consecutive windows. Equation 5 shows that e_Q and e_γ trade off with T_{m}. For achieving a certain level of error, the segments should be separated by the time of

$$T_{\mathrm{m}} \geq \frac{1}{\left(T_1 N_1\right)^{1/2}} \max\left\{ \frac{\sqrt{6}Q}{\pi e_Q B^{3/2}}, \frac{1}{|\gamma|e_\gamma \left(2B\right)^{1/2}} \right\} . \quad (6)$$

This limits the temporal resolution achievable in attenuation measurement and is inversely related to $1/Q$ and γ magnitude, e_Q and e_γ, frequency bandwidth as $B^{-3/2}$, segment length as $T_1^{-1/2}$ and selected peak number as $N_1^{-1/2}$. We use this constraint for determining the T_{m} to fulfil the accuracy with a certain error. For the identifying of sparse strongest reflections as in Figure 4, a certain length of data segment (T_{w} in Figure 4a) is required so that enough number of peaks can be achieved and stacked to suppress undesired effects such as from noise. This corresponds to equation 5 that larger N_1 leads to lower values of e_Q and e_γ.

With $T_m = 10$ ms, $B = |90 - 10| = 80$ Hz, $T_1 = 80$ ms and the situation of $N_1 = 16$ for the attenuation measurement on the walk-away DAS VSP data at the FRS in this report, the e_Q of estimated $1/Q$ around 0.12 as in Figure 8b is about 0.8 and e_γ of estimated γ around -25 s^{-1} as in Figure 8c is about 0.28 (equation 5). For the conservative relative standard error of $e_Q = e_\gamma = 0.3$, the shortest T_m required for this measurement is about 30 ms. Therefore, the attenuation estimation is not really detailed and accurate even with the high-quality high-resolution DAS VSP records. With the same T_1, N_1 and objective error of 0.3, the shortest T_m for $1/Q = 0.12$ is about 40 ms with $B = 60$ Hz, and for $1/Q = 0.02$ is about 250 ms with $B = 60$ Hz and is about 115 ms with $B = 100$ Hz. These results show the estimated attenuation is notably more confident with the broader bandwidth $B = |f_1 - f_2|$ available and better measurements can be attained where the attenuation is strong, which is in the situation of most attention (e.g. reservoir rock, CCS) in exploration seismology.

For real subsurface situation, different effects such as the one from closely spaced reflectivity (thin layer) can reduce the estimation accuracy and restrict the temporal resolution. Figure 9 simulates the thin-layer effect though synthetic wedge model. The model consists of 19 synthetic attenuated traces (black lines). Each trace is constructed by computing attenuation effects of constant $1/Q = 0.02$ and $\gamma = -2$ s^{-1} on unit pulses convolved with Ricker wavelet. We estimate the $1/Q$ and γ value (background color in Figure 9) for each trace of this wedge model by our method from the spectral ratio of estimated spectra and the spectrum of input Ricker wavelet. As shown in Figure 9, for traces 4 – 9 where the impulse responses are closely spaced, the estimated $1/Q$ and γ significant deviated from the input values. Note that the distortion of wavelet spectrum from this thin-layer effect cannot be eliminated in our estimation method.
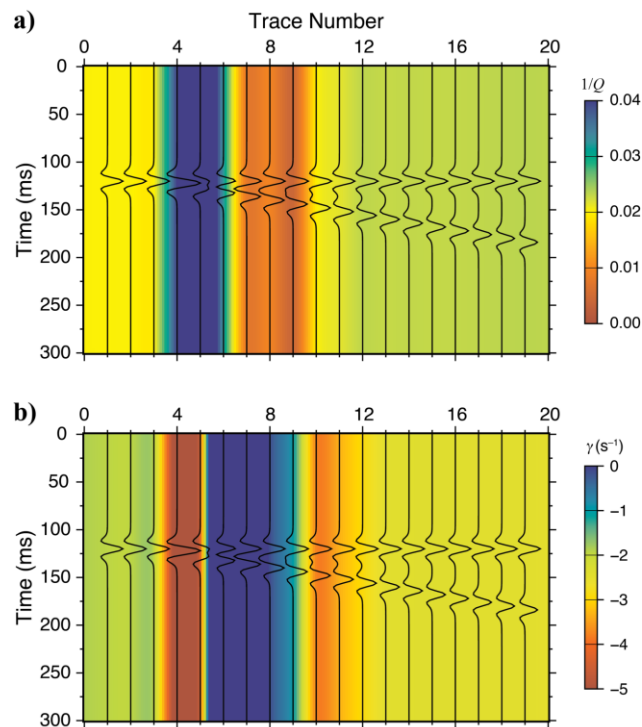

Figure 9. Synthetic wedge model (black lines) with (a) estimated $1/Q$ (background color) and (b) estimated γ (background color).

Shortest T_m for different $1/Q$ and bandwidth B, and tests on wedge model of Figure 9 all show that the attenuation measurement could be restrictive. The temporal resolution is sacrificed for achieving a certain accuracy or vice versa. This section also shows that 1) the accuracy of attenuation estimation strongly depends on the frequency bandwidth B and the $1/Q$ or γ value itself; 2) different effects such as the one from thin layer can reduce the accuracy of attenuation estimation which is also indistinguishable in principle from the effect of $1/Q$ and γ.

CONCLUISONS

Seismic attenuation is measured from the DAS VSP data at the CaMI FRS for monitoring the CO_2 injection. Large positive $1/Q$ and large negative γ of strong attenuation are shown around the CO_2 injection well at the injection zone of Basal Belly River Sandstone Formation. The attenuation measured through our approach of the stacking of sparse strongest reflections could thus be reliable CO_2 indicator. The calculations of the relative standard errors of $1/Q$ and γ also show that the attenuation measurement cannot be really accurate for achieving a certain temporal resolution. The temporal resolution of measurement needs to be sacrificed for getting a certain accuracy and vice versa.

ACKNOWLEDGEMENTS

REFERENCES

Behura, J.,and I. Tsvankin, 2009, Estimation of interval anisotropic attenuation from reflection data: Geophysics, 74, no. 6, A69– A74, doi:10.1190/1.3191733.

Carter, A. J., V. A. Torres Caceres, K. Duffaut, and A. Stovas, 2020, Velocity-attenuation model from check-shot drift trends in North Sea well data: Geophysics, 85, no. 6, D65–D74, doi: 10.1190/geo2019-0419.1.

Lawton, D. C., A. Gordon, S. Bidikhova, K. W. Hall, and M. B. Bertram, 2019, Update on DAS and geophone VSP surveys at the CaMI Field Research Station, Newell County, Alberta: CREWES Research Report, 31, 39.1–39.14.

Morozov, I. B., 2008, Geometric attenuation, frequency dependence of Q, and the absorption band problem: Geophysical Journal International, 175, 239–252, doi: 10.1111/j.1365-246X.2008.03888.x.

Neep, J. P., M. S. Sams, M. H. Worthington, and K. A. O'Hara-Dhand, 1996, Measurement of seismic attenuation from high-resolution crosshole data: Geophysics, 61, 1175–1188, doi: 10.1190/1.1444037.

O'Doherty, R. F., and N. A. Anstey, 1971, Reflections on amplitudes: Geophysical Prospecting, 19, 430–458, doi: 10.1111/j.1365-2478.1971.tb00610.x.

Reine, C., M. van der Baan, and R. Clark, 2009, The robustness of seismic attenuation measurements using fixed- and variable-window time-frequency transforms: Geophysics, 74, no. 2, WA123–WA135, doi: 10.1190/1.3043726.

Smith, W. H. F., and P. Wessel, 1990, Gridding with continuous curvature splines in tension: Geophysics, 55, 293-305, doi: 10.1190/1.1442837.

Sun, X., X. Tang, C. H. Cheng, and L. N. Frazer, 2000, P- and S- wave attenuation logs from monopole sonic data: Geophysics, 65, 755-765, doi: 10.1190/1.1444774.

Tonn, R., 1991, The determination of seismic quality factor Q from VSP data: A comparison of different computational methods: Geophysical Prospecting, 39, 1-27, doi: 10.1111/j.1365-2478.1991.tb00298.x.

Wang, Y., and I. B. Morozov, 2020, A simple approach to nonstationary source waveform estimation in seismic records: Geophysics, 85, no. 3, V257–V268, doi: 10.1190/geo2019-0133.1.

White, R. E., 1992, Accuracy of estimating Q from seismic data: Geophysics, 57, 1508–1511, doi: 10.1190/1.1443218.